Decadal Evolution of Supraglacial Hydrology on the Nivlisen Ice Shelf: From Localized Ponding to Spatially Synchronized Hydrofracture Forcing (2015-2026)

Geetha Priya M*, Charu Prabha R P, Y Mallikarjuna Madhav, Adithya Sunil, Raina Bharathi, Deva Jefflin A R

Centre for Incubation Innovation Research and Consultancy (CIIRC), Jyothy Institute of Technology, Bengaluru 560082, Karnataka, India

*Corresponding author email id: geetha.sri82@gmail.com

Abstract

Understanding the mechanical response of Antarctic ice shelves to surface meltwater is critical for evaluating their structural stability. This study presents 11 austral summer seasons (AS 2015-2016 to AS 2025-2026) assessment of supraglacial melt pond dynamics and their mechanical implications for the Nivlisen Ice Shelf grounding zone using Landsat-8/9 imagery combined with in-situ validation from the 44th Indian Scientific Expedition to Antarctica (ISEA-44). Supraglacial melt pond depths were retrieved from multispectral imagery and integrated into an Euler–Bernoulli flexural framework to estimate bending stresses, hydrostatic forcing, and the resulting stress intensity factors (K_{total}) across a network of ten major ponds. Two prominent hydrological events were identified: an extreme localized ponding episode in 2017 (maximum depth 6.92 m) and a spatially extensive meltwater event in January 2026 characterized by high thickness normalized energy (E_n = 97.81 MJ m^{-1}). Field validation using a Keller DCX-22 pressure transducer indicates that satellite retrievals underestimate pond depth by approximately 27.6% due to spatial averaging within 30 m pixels over concave pond bathymetry. Despite this conservative bias, calculated stress intensities reach up to 0.61 MPa $m^{1/2}$, exceeding the commonly reported fracture toughness range for glacier ice (0.1-0.4 MPa $m^{1/2}$). These results suggest that episodic supraglacial melt ponding can generate stress conditions favorable for hydrofracture initiation in the Nivlisen grounding zone sector. The study demonstrates the value of combining long-term satellite observations with field validation to assess the evolving mechanical vulnerability of Antarctic ice shelves.

Keywords: East Antarctica, Nivlisen Ice Shelf, Hydrofracture, Supraglacial melt pond, Stress intensity factor.

1. Introduction

Ice shelves are floating extensions of the Antarctic Ice Sheet that play a critical role in regulating the discharge of grounded ice into the ocean. By exerting a buttressing force on upstream glaciers, ice shelves slow the flow of inland ice and thereby help stabilize the Antarctic Ice Sheet. When ice shelves weaken or collapse, this buttressing effect is reduced, allowing glaciers to accelerate and potentially increasing contributions to global sea level rise (Morlighem et al., 2019; T. A. Scambos et al., 2004). One of the processes increasingly recognized as a key driver of ice shelf instability is the formation and drainage of supraglacial meltwater ponds and lakes. These surface water bodies can influence the mechanical stability of ice shelves by promoting fracture propagation through hydrofracture processes (Banwell et al., 2013; Bell et al., 2018).

Supraglacial melt ponds form when surface meltwater accumulates in topographic depressions on glaciers or ice shelves during the austral summer melt season. The occurrence and distribution of these lakes are controlled by surface energy balance, local topography, snow permeability, and the presence of pre existing fractures (Jonathan Kingslake, 2017; Stokes et al., 2019). Satellite observations have revealed widespread seasonal development of supraglacial melt ponds across both the Antarctic and Greenland ice sheets, with increasing evidence that their spatial extent and frequency are sensitive to climatic variability and atmospheric warming (Arthur et al., 2020; Langley et al., 2016; Murugesan et al., 2023). In Antarctica, supraglacial melt ponds have been observed across several ice shelves in East and West Antarctica, including the Amery, Shackleton, Roi Baudouin, and Larsen ice shelves (Arthur et al., 2020; Bell et al., 2017; Geetha Priya & Venkatesh, 2024). These lakes can store significant volumes of meltwater and may persist for extended periods before draining suddenly through fractures.

The mechanical influence of supraglacial melt ponds on ice shelves arises primarily from two mechanisms. First, the weight of ponded water imposes a vertical load on the ice surface, generating flexural stresses within the ice shelf. Second, when water infiltrates surface crevasses, the hydrostatic pressure of the water column can drive crack propagation through the ice. This process, known as hydrofracture, occurs when water pressure within a fracture exceeds the resisting stresses of the surrounding ice and allows the fracture to propagate downward through the ice column (Alley et al., 2005; Veen, 1998). Hydrofracture has been implicated as a key mechanism in the disintegration of several Antarctic ice shelves, most

notably the collapse of the Larsen B Ice Shelf in 2002, where extensive surface meltwater ponding preceded rapid structural failure (Ayeal et al., 2003; T. A. Scambos et al., 2000) .

The propagation of fractures in ice is commonly analyzed using the framework of linear elastic fracture mechanics (LEFM), in which the stress intensity factor (SIF) describes the magnitude of stress concentration at the tip of a crack (Anderson, 2017). Fracture propagation occurs when the applied stress intensity exceeds the fracture toughness of the material, denoted as (K_{IC}). Laboratory and field measurements indicate that the fracture toughness of glacier ice typically lies in the range of approximately 0.1–0.4 MPa $m^{1/2}$, depending on temperature, grain size, and loading conditions (Rist et al., 2002; Schulson, 2011). In the context of supraglacial hydrology, the total stress intensity acting at a crevasse tip may arise from multiple sources, including bending stresses generated by pond loading, hydrostatic pressure from water filling the crevasse, and the opposing lithostatic stress associated with the weight of the overlying ice column.

Recent studies have highlighted the importance of understanding the coupling between supraglacial hydrology and fracture mechanics in determining the structural stability of ice shelves. Observational analyses have documented rapid drainage of supraglacial melt ponds through hydrofracture, demonstrating that meltwater can penetrate through hundreds of meters of ice within short timescales (Banwell et al., 2013; Lai et al., 2020). Numerical modelling and remote sensing studies further suggest that increasing surface melt under a warming climate could enhance hydrofracture susceptibility across several Antarctic ice shelves (Bell et al., 2018; Pollard & Deconto, 2016). These findings underscore the need for quantitative assessments of the mechanical forcing generated by supraglacial meltwater and its potential to initiate fracture propagation.

Despite these advances, relatively few studies have combined observations of supraglacial melt pond geometry with fracture mechanics based calculations to evaluate the stress intensities generated by meltwater loading. Such analyses are important for determining whether supraglacial melt ponds generate stresses capable of exceeding the fracture toughness of ice and thus triggering hydrofracture. In this study, we investigate the fracture mechanical implications of supraglacial melt pond loading by quantifying the gravitational potential energy (GPE) associated with meltwater ponds and evaluating the resulting SIF acting on surface fractures. By integrating satellite derived pond geometry with physically based calculations of bending stresses, hydrostatic water pressure and lithostatic resistance, this work provides a

process-based assessment of the hydrofracture potential of supraglacial melt ponds and their implications for the structural stability of Antarctic ice shelves.

2. Study Area

The study is carried out on the Nivlisen Ice Shelf (NIS), located in Central Dronning Maud Land (cDML), East Antarctica, in the vicinity of the Schirmacher Oasis along the Princess Astrid Coast (Figure 1). cDML is a climatically and logistically well documented sector of East Antarctica and hosts several long-term glaciological and geophysical observations, making it particularly suitable for process oriented studies of ice ocean atmosphere interactions and ice shelf stability (K. Mahalinganathan et.al, 2011).

A total of ten supraglacial melt ponds were selected on the NIS and labelled P1–P10. All ponds exhibit irregular polygonal planform geometries and have end-to-end (maximum Feret) diameters exceeding 250 m. This minimum diameter threshold of 0.25 km follows previous hydrofracture and surface melt studies, which indicate that lakes of this linear scale are more likely to contain the water volume necessary to generate mechanically significant water loading or sustained fracture propagation (T. A. Scambos et al., 2000).

The distance of each pond from the grounding line was calculated as the shortest perpendicular distance from the pond centroid to the nearest mapped grounding line. The selected ponds are situated between 242 m (P9) and 2,791 m (P1) from the grounding line, thereby sampling a mechanical gradient across the near-field sector of the ice shelf (Table 1). This configuration is specifically designed to investigate hydrofracture processes ranging from the high flexure grounding line (P9) to the outer limit of the grounding zone's mechanical influence (P1), rather than the freely floating interior of the shelf.

NIS in cDML was selected because multiple supraglacial melt ponds occur within a few kilometres of a well defined grounding line, enabling a focused assessment of hydrofracture under strong grounding zone bending stresses. In addition, this study is uniquely supported by in-situ pond water depth and hydrostatic pressure measurements acquired during ISEA-44 (November 2024-January 2025) with logistics provided by National Centre for Polar and Ocean Research (NCPOR) under the Ministry of Earth Sciences (MoES), Government of India (GoI), which allows direct physical constraint of co-incident satellite based hydrofracture modelling, ensuring that the simulated fracture mechanics are validated against real time bathymetric and pressure states.

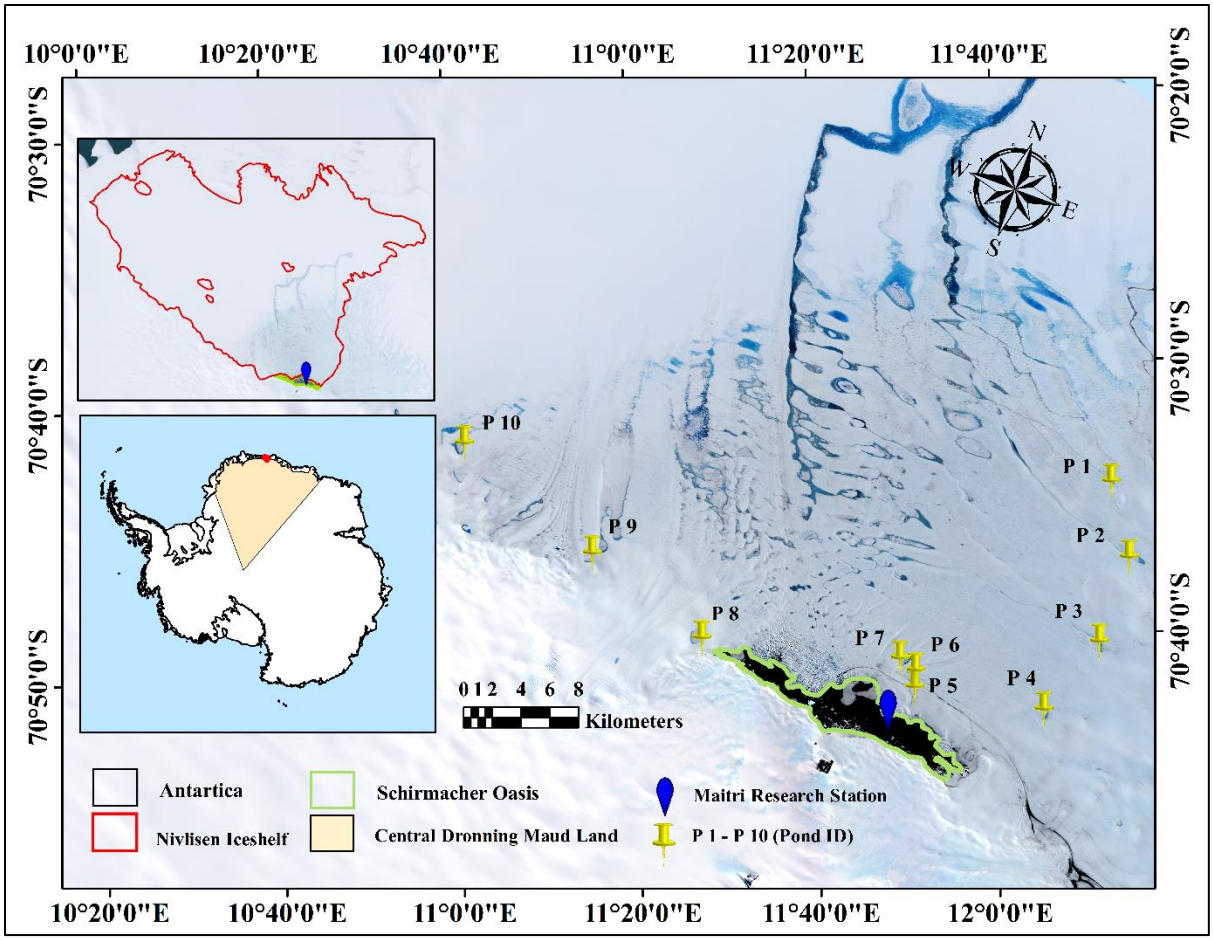

Figure 1. Study area map showing the location of selected 10 supraglacial melt ponds on the NIS, cDML, East Antarctica. (Base map- Landsat-8 imagery acquired on 28-01-2020)

Table 1. Distance of supraglacial melt ponds from the grounding line and corresponding local ice thickness derived from BedMachine v2.

S.no	Pond ID	Latitude, Longitude	Distance to the grounding line (m)	Local ice thickness (m)
1	P 1	-70.582477,12.054874	2791	519
2	P 2	-70.626066,12.129485	1979	655
3	P 3	-70.683820,12.093088	1007	639
4	P 4	-70.732944,12.016636	725	583
5	P 5	-70.729622,11.759308	651	393
6	P 6	-70.718715,11.755004	1161	409
7	P 7	-70.713614,11.736857	1337	390
8	P 8	-70.729676,11.335885	2296	446
9	P 9	-70.694339,11.112440	242	317
10	P 10	-70.640898,10.829409	1238	348

3. Data used

3.1 Satellite imagery and pond mapping

We analyzed 11 austral summer seasons (AS 2015-2016 to AS 2025-2026) using 19 cloud free scenes from Landsat-8 Operational Land Imager (OLI), Landsat-9 OLI2. Scenes were filtered for a maximum of 20% total scene cloud cover, with manual inspection conducted to ensure all 10 target pond locations were cloud free in the selected acquisitions (Table 2).

The dataset distribution varies from one scene per season in the early study period to four scenes per season in later years (Table 3). This multi temporal approach captures the ponds at various stages of the melt cycle from November through February. In Table 3, "undetected pond IDs" refers specifically to cloud obscuration or extensive fresh snow cover preventing a clear observation of the ice surface, this distinction is critical to avoid underestimating pond frequency in the presence of seasonal weather patterns (Arthur et al., 2020; Geetha Priya et al., 2022). To delineate pond boundaries and estimate depth, we utilized the Blue (band 2) and Red (band 4) 30 m resolution bands. Specifically, we calculated the Normalized Difference Water Index for ice ($NDWI_{ice}$) using both bands for robust surface water masking, while the Red band was utilized for the radiative transfer model (RTM) for water depth estimation, following the optimized single band approach for supraglacial melt ponds on East Antarctic ice shelves. Sentinel-1 SAR imagery (C-band) from February 2015 onward was examined to assess the persistence of supraglacial drainage structures across austral summer seasons.

3.2 Ice thickness and BedMachine integration

Ice thickness (H) for each pond centroid was extracted from the BedMachine Antarctica v2 dataset (Morlighem et al., 2019). While BedMachine provides a 500 m gridded product, thickness values were extracted using bilinear interpolation to derive thickness values specifically at the pond centroids, minimizing discretization artifacts that arise when applying a 500 m regional grid (BedMachine) to 250 m scale surface features.

We assigned a single, time invariant thickness value and grounding line position to each pond for the duration of the study period. This assumption of stationarity is justified by the glaciological stability of the NIS, which is characterized by slow flow velocities and negligible multi year thickness changes in cDML (K. Mahalinganathan et.al, 2011; Morlighem et al., 2019). Interannual thinning and grounding line migration in this sector are significantly smaller than the inherent vertical uncertainty of the BedMachine product and the 30 m horizontal

resolution of the satellite imagery used for pond mapping. Consequently, these variations are treated as secondary to the high frequency hydrostatic and flexural stresses that drive seasonal hydrofracture, allowing for a consistent spatial baseline across the study period (Banwell et al., 2013).

Table 2. Landsat scenes used for supraglacial melt pond analysis, including satellite platform, product level, acquisition date, scene ID, path and row.

S.No	Satellite	Date	Scene_ID	Path	Row
1	LC08	01-01-2016	LC08_L1GT_167110_20160101_20201016_02_T2	167	110
2	LC08	21-12-2017	LC08_L2SR_167110_20171221_20201016_02_T2	167	110
3	LC08	04-02-2017	LC08_L2SR_167110_20170204_20201016_02_T2	167	110
4	LC08	24-12-2018	LC08_L2SR_167110_20181224_20201016_02_T2	167	110
5	LC08	28-01-2020	LC08_L2SR_167110_20200128_20201016_02_T2	167	110
6	LC08	13-12-2020	LC08_L2SR_167110_20201213_20210314_02_T2	167	110
7	LC08	10-01-2021	LC08_L2SR_167110_20210114_20210308_02_T2	167	110
8	LC08	14-11-2021	LC08_L2SR_167109_20211114_20211125_02_T2	167	110
9	LC09	24-12-2021	LC09_L2SR_167110_20211224_20230503_02_T2	167	110
10	LC09	25-11-2022	LC09_L1GT_167109_20221125_20230320_02_T2	167	110
11	LC09	27-12-2022	LC09_L1GT_167110_20221227_20230316_02_T2	167	110
12	LC09	28-01-2023	LC09_L1GT_167109_20230128_20230309_02_T2	167	110
13	LC08	21-02-2023	LC08_L1GT_167110_20230221_20230228_02_T2	167	110
14	LC09	30-12-2023	LC09_L1GT_167110_20231230_20231230_02_T2	167	110
15	LC08	01-07-2024	LC08_L1GT_167109_20240107_20240122_02_T2	167	110
16	LC08	24-02-2024	LC08_L2SR_167109_20240224_20240229_02_T2	167	110
17	LC08	09-01-2025	LC08_L1GT_167110_20250109_20250121_02_T2	167	110
18	LC09	19-12-2025	LC09_L2SR_167110_20251219_20251220_02_T2	167	110
19	LC09	06-01-2026	LC09_L2SR_165110_20260106_20260107_02_T2	165	110

Table 3. Temporal record of satellite observations and visibility of supraglacial melt ponds during the study period.

Year	Date	Undetected Pond IDs
AS 2015-2016	01-01-2016	P 1,P6
AS 2020-2021	13-12-2020	P 5,P 6
AS 2020-2021	14-01-2021	P 1,P 5
AS 2021-2022	14-11-2021	P 1,P 3, P 5,P 6,P 10
AS 2022-2023	25-11-2022	P 1,P 10
AS 2022-2023	21-02-2023	P 1,P5
AS 2023-2024	12-11-2023	P 1,P 10
AS 2023-2024	30-12-2023	P 1,P 5,P 10
AS 2023-2024	07-01-2024	P 1,P 10
AS 2023-2024	24-02-2024	P 5,P 10

4. Methodology: Satellite preprocessing and melt-pond depth retrieval

The hydrofracture analysis was carried out for ten supraglacial melt ponds on the NIS, located near the Schirmacher Oasis, using multisensor satellite observations and a two-dimensional LEFM framework (Figure 2).

Surface reflectance Landsat-8, 9 scenes acquired during 11 austral summers were radiometrically and atmospherically pre processed. Melt pond depths (h) were retrieved following the RTM (equation 1) together with the $NDWI_{ice}$ formulation (equation 2) and threshold values reported in the same study (Arthur et al., 2020; Geetha Priya et al., 2022).

$$h = \frac{[\ln(A_v - R_d) - \ln(R_w - R_d)]}{c} \quad (1)$$

$$NDWI_{ice} = \frac{(\text{Blue band}_{\text{reflectance}} - \text{Red band}_{\text{reflectance}})}{(\text{Blue band}_{\text{reflectance}} + \text{Red band}_{\text{reflectance}})} \quad (2)$$

Where, A_v is the average reflectance around pond boundary, R_d is the deep water reflectance (~0), R_w is the shallow water reflectance, c is the attenuation coefficient.

Additionally, $NDWI_{ice}$ thresholded rasters were converted to pond polygons in QGIS (Quantum Geographic Information System) and used to mask the corresponding depth rasters. Zonal statistics were then computed for each pond to obtain area, maximum depth, mean depth, and pixel integrated water volume. To ensure bathymetric consistency across the 30 m resolution grid, anomalous depth outliers were identified via the depth standard deviation and removed prior to selecting final maximum depth values. The derived pond geometries and bathymetric

profiles serve as the primary inputs for the hydrofracture modelling framework, integrated with the crack depth scenarios described below.

4.1 Pre-existing crevasse assumption

In this study, the terms crevasse, crack, and fracture refer to the same surface initiated tensile discontinuity within the ice column. A pre existing near-surface crevasse is assumed to exist beneath each supraglacial melt pond. Observational and theoretical studies show that supraglacial melt ponds often occupy mechanically weakened or pre fractured zones and may activate near surface crevasses during hydrofracture initiation (Banwell et al., 2013; T. Scambos et al., 2009). The repeated formation of the same ponds across multiple austral summers in our dataset suggests the presence of persistent structural weaknesses, supporting this assumption.

As the subsurface geometry cannot be directly observed, the crack configuration is prescribed following first order fracture mechanics treatments (Veen, 1998). We assume the crevasse initially exists as a dry fracture. When a pond forms above it, water is assumed to infiltrate and hydraulically connect with the crevasse. This converts the feature into a water filled fracture where the net stress intensity (K_{total}) is determined by the superposition of hydrostatic water pressure and the ambient glaciological stress field, specifically the bending induced tensile stresses characteristic of the grounding zone.

To evaluate the sensitivity of hydrofracture potential to these combined stresses, three crack-depth scenarios were considered: 10 m, 20 m, and 30 m. These represent (i) typical penetration of dry crevasses, (ii) deeper penetration approaching the firn ice transition and (iii) a depth at which water filled fractures may become mechanically unstable under the influence of flexural loading and hydrostatic head, following first order analyses (Veen, 1998).

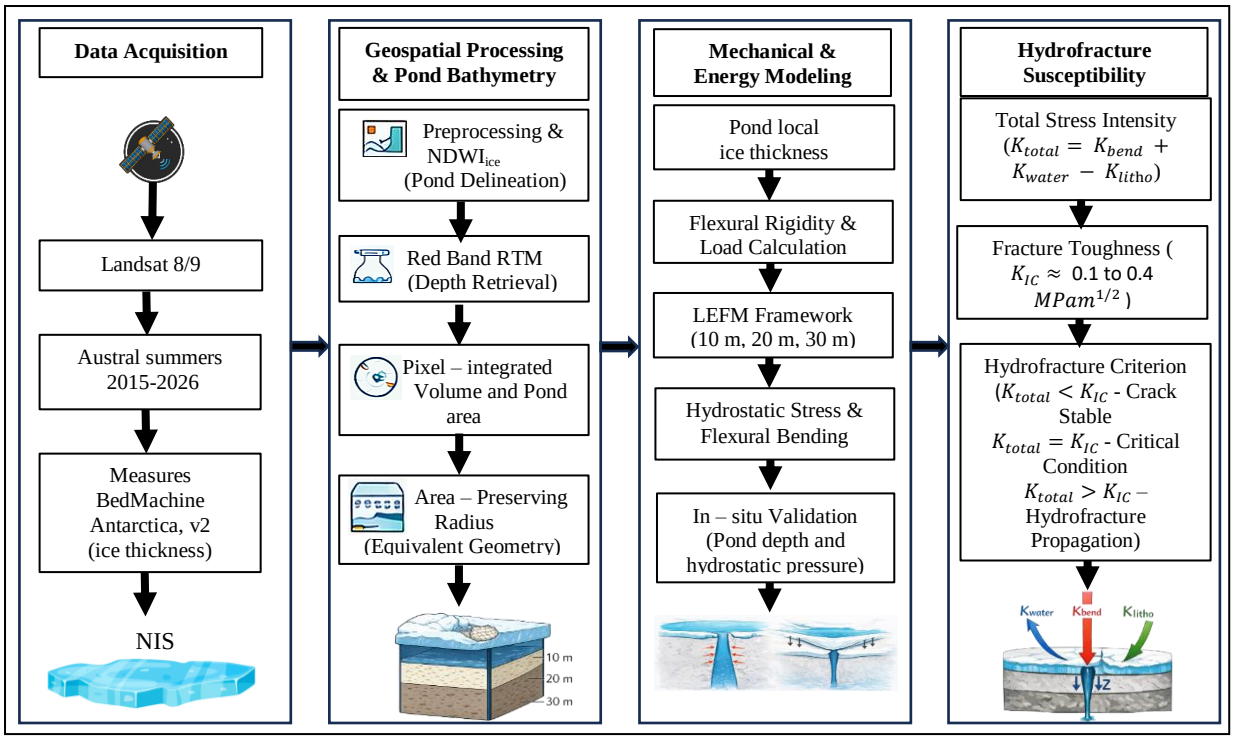

Figure 2. Process Flow

5. Hydrofracture modelling framework

5.1 LEFM formulation and plane strain assumption

A two-dimensional (2D) LEFM framework under plane strain conditions was used to evaluate the stability of the ten irregularly shaped melt ponds. This formulation is physically justified because observed pond diameters (>250 m) are an order of magnitude larger than the prescribed crack depths (10-30 m), allowing the central cross-section to be treated as effectively infinite in the out-of-plane direction (Krawczynski et al., 2009). The characteristic pond radius (r) is calculated from the area equivalent diameter (D_{eff}) (Equations 3-4) and used to define the lateral extent of the hydrostatic load. The 2D plane strain assumption provides a conservative estimate of the SIF by neglecting the three-dimensional "clamping" effects of a finite circular pond perimeter (Veen, 1998). LEFM is adopted in preference to viscous or viscoelastic formulations because the timescale of hydrofracture is significantly shorter than the Maxwell relaxation time of ice, such that the material response during loading is appropriately described as brittle elastic (Cuffey, 2011; Veen, 1998).

$$r = \frac{D_{eff}}{2} \quad (3)$$

$$D_{eff} = 2\sqrt{\frac{Pond\ Area}{\pi}} \quad (4)$$

5.2 Grounding line flexure and bending stresses

Although the study region lies approximately 50-90 km upstream of the calving front, all analysed ponds are located close to the southern grounding line (242-2,791 m). The ice shelf is therefore approximated as a clamped Euler-Bernoulli elastic beam within the grounding line flexure zone, where semi diurnal tidal deflections of approximately 1.5 m exert a first order control on the stress state of the ice shelf (G. Holdsworth, 1969; Vaughan, 1995). Due to the large flexural rigidity, small vertical deflections are amplified into significant surface tensile stresses at the grounding line hinge.

5.3 Material properties

To represent localized conditions near the Schirmacher Oasis, we adopted a depth averaged ice density (ρ_i) of 850 kg m^{-3} and a Young's modulus (E) of ~9 GPa (Nimmo, 2004; Sinharay, 2022). This density represents the depth integrated mean of the meteoric ice column, accounting for the suppression of deep firn by katabatic wind scouring (Humbert et al., 2009). The resulting stiff, brittle near-surface ice column is critical for assessing fracture initiation. The adopted E value lies within the upper range for polycrystalline ice consistent with Ground Penetrating Radar (GPR) and stratigraphy data from local blue ice areas (BIAs) (Cuffey, 2011; Sinharay, 2022). This depth averaged approach ensures a robust estimate of lithostatic overburden pressure (P_i) and resulting SIFs.

5.4 Hydraulic loading and stress-intensity formulation

For each pond, meltwater mass (M) and hydrostatic pressure (P_b) were calculated using a freshwater density of 1000 kg m^{-3}. The hydraulic driving force is governed by the total head, the sum of maximum retrieved pond depth h_{max} and the prescribed crack depth z. This total head determines the hydrostatic SIF K_{water} (Veen, 1998). Bending stresses σ_f are incorporated using a static bending coefficient C = 0.15. This formulation enables the explicit coupling of satellite derived bathymetry with ice geometry from BedMachine Antarctica v2 (Arthur et al., 2020; Morlighem et al., 2019; Murugesan et al., 2023). For each pond and crack depth scenario (10 m, 20 m, and 30 m), the formulations summarized in Table 4 adapted from established

studies were used to compute hydrostatic pressure at the pond bottom and crack tip, GPE and E_n along with surface load (q), flexural rigidity (D_f) and flexural length (l_f). Fracture stability was evaluated using the SIFs due to water loading (K_{water}), bending (K_{bend}), and lithostatic pressure (K_{litho}), which were summed to obtain the total SIF (K_{total}).

Table 4. Summary of governing equations used to derive hydraulic, mechanical, and fracture parameters within the supraglacial melt pond hydrofracture framework.

S. No	Parameter	Governing Equation	Where
1	Hydrostatic Pressure at Pond Bottom (kPa)	$Pb = \rho_w g\, h_{max}$	g = 9.81 m s^{-2}, h_{max}- maximum pond depth
2	Hydrostatic Pressure at Crack Tip (kPa)	$Pw = \rho_w\, g(z + h_{max})$	z - crack depth (assumed 10 m), h_{max} - maximum pond depth
3	Bending Stress (Pa)	$\sigma_f = \frac{6M_{max}}{H^2}$	M_{max}- maximum bending moment, H - ice thickness
4	Maximum Bending Moment (N)	$M_{max} = Cqr^2$ $If\ r < l_f \rightarrow M_{max} = 0.15qr^2;$ $If\ r \geq l_f \rightarrow M_{max} = 0.15q\ {l_f}^2$	q - surface load l_f - flexural length
5	Gravitational Potential Energy (J)	$GPE = \rho_w gVz$	
6	Driving Hydrofracture Energy (J)	$E_{drive} = GPE\left(\frac{P_b}{P_w}\right)$	P_b - hydrostatic pressure at pond bottom, P_w – hydrostatic pressure at crack tip
7	Thickness-Normalized Energy (J m^{-1})	$E_n = \frac{E_{drive}}{H}$	
8	Ice Overburden Pressure (kPa)	$P_i = \rho_i gz$	ρ_i - ice density (850 kg m^{-3}),
9	Surface load (Pa)	$q = \rho_w\, gh_{mean}$	H_{mean} - mean pond depth.
10	Flexural Rigidity (Nm)	$D_f = \frac{EH^3}{[12(1-\nu^2)]}$	E - Young's modulus (9×10^9 Pa), ν - Poisson's ratio (0.30)
11	Flexural Length (m)	$l_f = \left(\frac{D_f}{\rho_w g}\right)^{\frac{1}{4}}$	D_f - flexural rigidity
12	SIF from Bending (MPa m$^{1/2}$)	$K_{bend} = 1.12\ \sigma_f \sqrt{\pi z}$	σ_f - bending stress,
13	SIF from Water Pressure (MPa m$^{1/2}$)	$K_{water} = \left[1.12(\rho_w\, g\, h_{max}) + \left(\frac{2}{\pi}\right)\rho w\, g(z)\right]\sqrt{\pi z}$	h_{max} - maximum pond depth
14	SIF from Lithostatic Pressure (MPa m$^{1/2}$)	$K_{litho} = \left[\left(\frac{2}{\pi}\right)\rho_i gz\right]\sqrt{\pi z}$	
15	Combined Stress Intensity Factor (MPa m$^{1/2}$)	$K_{total} = K_{bend} + K_{water} - K_{litho}$	K_{bend} - SIF from bending, K_{water}- SIF from water pressure, K_{litho}- SIF from lithostatic pressure

6.Results

This section presents the morphometric, hydraulic and mechanical findings for the ten supraglacial melt ponds. Following the methodology established in Section 4, all parameters were evaluated across three crack depth scenarios (10 m, 20 m, and 30 m). This sensitivity framework allows for a direct comparison between the initial fracture state (10 m) and

progressive hydrofracture scenarios (20-30 m), illustrating the shifting balance between lithostatic overburden and hydrostatic driving pressure. These results are detailed across Sections 6.1-6.6.

6.1 Morphometric and bathymetric characteristics of supraglacial melt ponds

Across 11 AS seasons, the ten analysed supraglacial melt ponds exhibit pronounced spatial and temporal variability in surface area, depth, and water volume (Table 5; Figure 3). Individual ponds were detected between 11 observations (P1) and 19 observations (P2, P4, P8, and P9), reflecting differences in seasonal persistence as well as occasional cloud or snow obscuration in the satellite record. Mean pond surface areas vary substantially between ponds, ranging from 0.33 km² (P6) to 1.20 km² (P2). The largest individual pond recorded during the study period occurred at P2, which reached 1.53 km² on 9 January 2025. Several other ponds exhibit consistently large extents, particularly P3, P4, and P8, which maintain mean surface areas exceeding 0.75 km² throughout the observation period. These observations indicate that the NIS hosts multiple large and persistent supraglacial melt ponds capable of storing substantial meltwater. Maximum pond depth (h_{max}), retrieved using the RTM varies considerably among ponds and between seasons. The mean of the seasonal maximum depths for individual ponds ranges from 0.93 m (P3) to 1.49 m (P5). The deepest individual water column in the dataset occurs at P10, reaching 6.92 m on 4 February 2017. Other episodically deep ponds include P9 (5.43 m on 6 January 2026) and P4 (4.33 m on 28 January 2023), demonstrating that significant deepening events can occur even in ponds that are not among the largest by area. Meltwater storage volumes (V) show strong inter pond variability. Mean pond volumes range from 0.13×10^6 m^3 (P10) to 0.38×10^6 m^3 (P4). The largest individual water volume recorded in the dataset occurs at P4, which reached 1.48×10^6 m^3 on 21 December 2017, followed by P8, which stored 1.26×10^6 m^3 on 6 January 2026. These mean and maximum volumes represent statistics computed from all individual satellite observations available for each pond. Spatially, ponds with the largest areas and volumes occur across the grounding zone sector (242-2,791 m downstream of the hinge). While large ponds such as P2, P3, P4, and P8 are characterized primarily by extensive surface area and storage capacity, smaller pond such as P10 which functions as a steep sided "well" or "moulin-like" feature can develop episodically deep water columns. This highlights the importance of local pond geometry in controlling meltwater accumulation on the NIS.

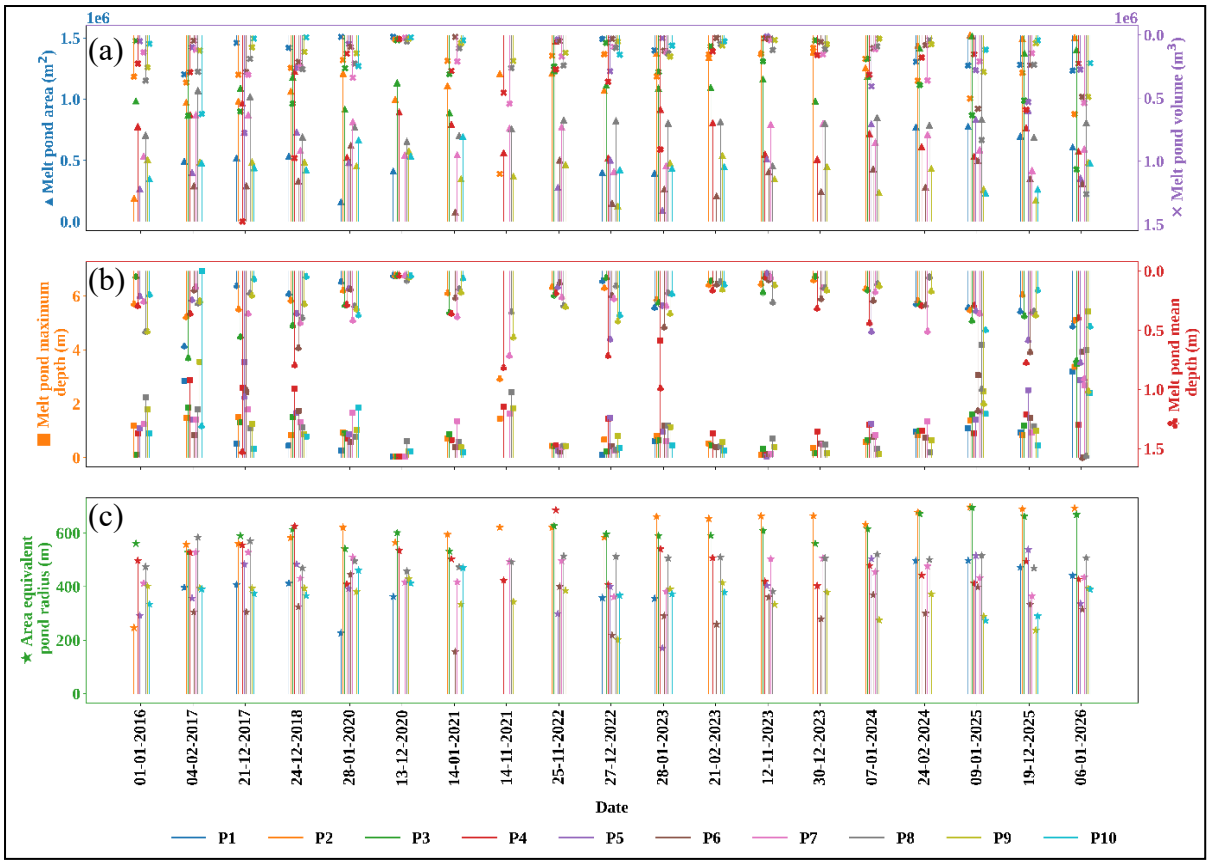

Figure 3. Temporal evolution of supraglacial melt pond geometry over eleven austral summers: (a) area and volume, (b) maximum and mean depth, and (c) area-equivalent radius.

Table 5. Morphometric and bathymetric characteristics of supraglacial melt ponds on the NIS during the study period.

S.no	Pond ID	Mean Area (km^2)	Max Area (km^2)	Mean h_{max} (m)	Max h_{max} (m)	Mean Volume (km^3)	Max Volume (km^3)
1	P1	0.52	0.78	1	3.18	0.14	0.31
2	P2	1.2	1.53	0.95	3.37	0.31	0.63
3	P3	1.14	1.52	0.93	3.48	0.34	1.07
4	P4	0.77	1.48	1.38	4.34	0.38	1.48
5	P5	0.53	0.91	1.49	3.54	0.24	0.78
6	P6	0.33	0.62	1.18	3.92	0.16	0.59
7	P7	0.65	0.87	1.1	2.68	0.22	0.55
8	P8	0.78	1.07	1.27	4.2	0.26	1.26
9	P9	0.41	0.58	1.27	5.43	0.14	0.49
10	P10	0.45	0.69	1.3	6.92	0.13	0.63

317

318 **6.2 Derived hydraulic and geometric properties**

319 Using the geometries derived for the ten ponds (2015-2026), area equivalent radii (r)
320 were computed for each observation to serve as the lateral scale for water loading in the LEFM
321 formulation (equations 3-4). The radii range from 157 m (for P6 on 14 January 2021) to 697 m
322 (for P2 on 9 January 2025) (Table 6). Because these diameters are significantly larger than the
323 assumed crack depths (10-30 m), the conditions for the plane strain approximation are satisfied
324 (Veen, 1998).

325 Meltwater mass (M), derived using a freshwater density of 1000 kg m^{-3}, varies from 1.05 x 10^1
326 kt (for P5 on 12 November 2023) to 1.48 x 10^3 kt (for P4 on 21 December 2017). This mass
327 serves as the surface load for calculating flexural stresses. The total hydraulic head (H_w) acting
328 within the fracture is defined as the sum of maximum pond depth and crack depth ($H_w = h_{max}$
329 + z) (Krawczynski et al., 2009; Veen, 1998). For the 10 m baseline, H_w ranges from 10.04 m
330 (for P2 on 13 December 2020) to 16.92 m (for P10 on 4 February 2017). At 30 m depth, H_w
331 increases to a maximum of 36.92 m. These water columns generate substantial hydrostatic
332 pressures. The pressure at the pond base (P_b) varies between 0.35 kPa (for P2 on 13 December
333 2020) and 67.93 kPa (for P10 on 4 February 2017). At the crack tip, pressure (P_w) increase
334 systematically with depth. For the 10 m scenario, P_w ranges from 98.45 kPa (for P2 on 13
335 December 2020) to 166.03 kPa (for P10 on 4 February 2017) as shown in Figure 4. For the 20
336 m and 30 m scenarios, pressure increase to 196.55 to 264.13 kPa and 294.65 to 362.23 kPa
337 respectively. The peak pressure consistently occurs at P10, reflecting its role as a deep
338 hydrostatic "well." These values provide the boundary inputs for the stress intensity analysis
339 in the following sections.

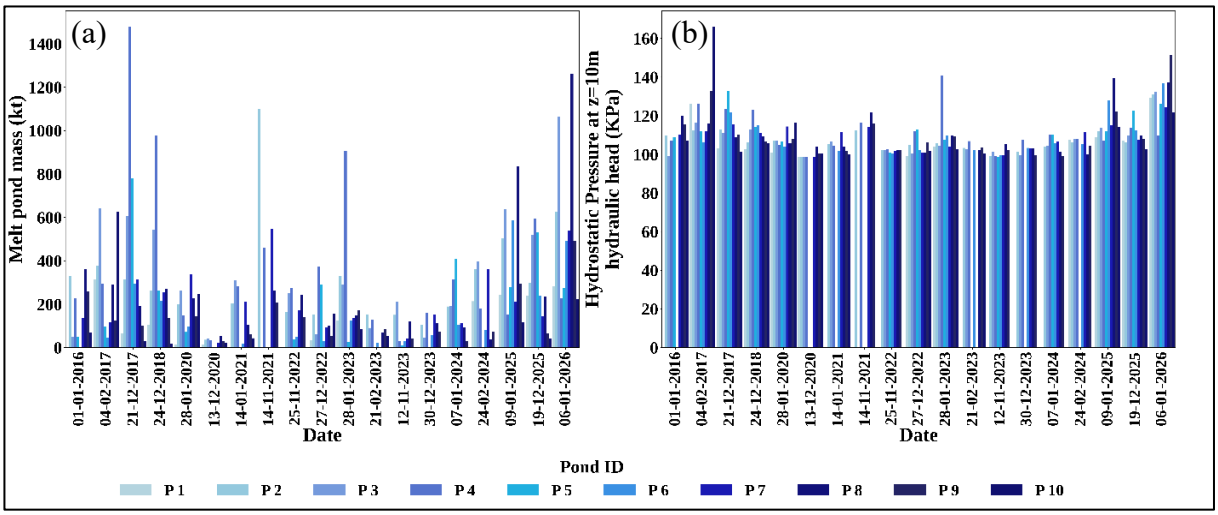

Figure 4. Temporal variability of (a) meltwater mass and (b) hydrostatic pressure at the crack tip (z = 10 m hydraulic head).

Table 6. Min/max hydraulic and geometric parameters for melt ponds P1-P10

S.no	Parameter	Min value	Pond ID	Date	Max value	Pond ID	Date
1	Area-equivalent pond radius	157 m	P6	14-01-2021	697 m	P2	09-01-2025
2	Meltwater mass	1.05×10^{1} kt	P5	12-11-2023	1.48×10^{3} kt	P4	21-12-2017
3	Hydraulic head (10 m crack)	10.04 m	P2	13-12-2020	16.92 m	P10	04-02-2017
4	Hydraulic head (20 m crack)	20.04 m	P2	13-12-2020	26.92 m	P10	04-02-2017
5	Hydraulic head (30 m crack)	30.04 m	P2	13-12-2020	36.92 m	P10	04-02-2017
6	Hydrostatic pressure (pond base)	0.35 kPa	P2	13-12-2020	67.93 kPa	P10	04-02-2017
7	Crack-tip pressure (10 m crack)	98.45 kPa	P2	13-12-2020	166.03 kPa	P10	04-02-2017
8	Crack-tip pressure (20 m crack)	196.55 kPa	P2	13-12-2020	264.13 kPa	P10	04-02-2017
9	Crack-tip pressure (30 m crack)	294.65 kPa	P2	13-12-2020	362.23 kPa	P10	04-02-2017

6.3 Flexural and mechanical response to supraglacial melt pond loading

The mechanical response of the NIS was quantified using surface water loads, bending moments (Mmax), and bending stresses (σf) derived for individual observations between 2015 and 2026 (Table 7; Figure 5). These parameters define the elastic flexure induced by the hydrostatic weight of ponded meltwater.

6.3.1 Surface loading and bending moments

Surface loading spans nearly two orders of magnitude across the dataset. The lowest load occurs for P5 (202 Pa on 12 November 2023), while the highest reaches 1.55×10^4 Pa (for P6 on 6 January 2026) reflecting extensive supraglacial meltwater accumulation. Several seasons exhibit particularly strong mechanical forcing. For example, the AS of 21 December 2017 shows elevated loads across multiple ponds, including P4 (1.50×10^4 Pa) and P5 (1.04×10^4 Pa).

This variability is mirrored in the maximum bending moments (M_{max}), which reflect seasonal meltwater production and pond geometry. The smallest moment was recorded at P5 on 12 November 2023 (4.93×10^6 N), whereas the largest historically occurred at P4 on 21 December 2017 (6.93×10^8 N). The 6 January 2026 event marks a significant intensification of mechanical forcing compared to the relatively stable 2020-2025 period, with bending moments reaching 5.92×10^8 N at P8 and 4.99×10^8 N at P3. These 2026 values represent a sharp intensification of mechanical forcing compared to the relatively stable years of 2020-2025, signalling a return to conditions that favor structural instability.

6.3.2 Bending stress and spatial rigidity

The bending moments (σ_f) translate into surface tensile stresses that contribute to fracture initiation. Across all observations, σ_f remains below the typical tensile strength of glacier ice (approximately 0.7-1.0 MPa), but fluctuates significantly. The maximum bending stress in the dataset occurs at P9 on 24 December 2018 (3.77×10^{-2} MPa). While 2018 produced the single highest localized stress, the 6 January 2026 season represents a more spatially extensive event; several ponds simultaneously experienced elevated stresses, including P8 (1.78×10^{-2} MPa) and pond P9 (1.37×10^{-3} MPa). This spatially coherent loading affects a larger portion of the shelf surface simultaneously, which may be more critical for overall stability than isolated maxima.

These responses are governed by the shelf's elastic properties. Flexural rigidity varies between 2.63×10^{16} Nm (for P9 on 6 January 2026) and 2.32×10^{17} Nm (for P2 on 1 January 2016), reflecting spatial differences in ice thickness and stiffness. The corresponding flexural length

ranging from 1280 m (P9) to 2205 m (P2) remains constant for each pond location, confirming that the mechanical sensitivity of each pond is pre determined by its glaciological position relative to the grounding line.

6.3.3 Mechanical implications for stability

The extreme ponding events of December 2017, 2018 and January 2026 represent peak periods of mechanical forcing. While the 2017 event produced the largest bending moments (structural deformation), the 2018 event maximized localized bending stress (fracture risk). Crucially, the 2026 event demonstrates a widespread mechanical response across ponds P3, P6, P7, P8, P9, and P10 (Table 7). Although individual bending stresses remain an order of magnitude below the failure threshold for intact ice, such repeated seasonal loading progressively modifies the local stress field (Banwell et al., 2013; Veen, 1998). When these flexural stresses are coupled with high internal water pressures, as seen in the 2017 and 2026 seasons, the conditions for hydrofracture initiation and the reactivation of dormant surface fractures are significantly enhanced.

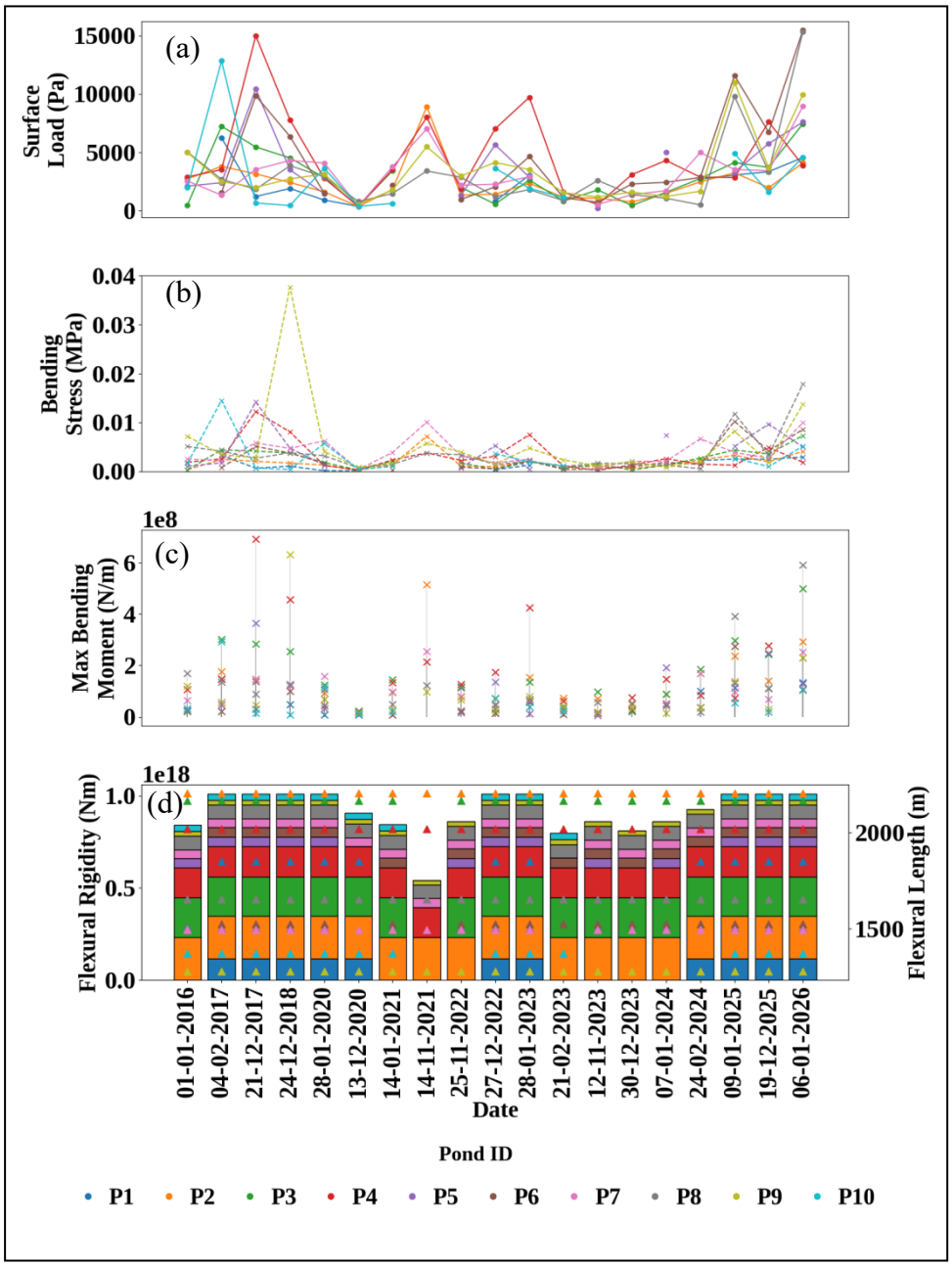

Figure 5. Mechanical response to supraglacial melt pond loading over eleven austral summers: (a) surface load, (b) bending stress, (c) maximum bending moment, and (d) flexural rigidity and flexural length.

437 **Table 7.** Mechanical parameters associated with supraglacial melt pond loading.

S.no	Parameter	Min value	Pond ID	Date	Max value	Pond ID	Date
1	Surface load	202 Pa	P5	12-11-2023	1.55×10^4 Pa	P6	06-01-2026
2	Maximum bending moment	4.93×10^6 N m^{-1}	P5	12-11-2023	6.93×10^8 N m^{-1}	P4	21-12-2017
3	Bending stress	1.54×10^{-4} MPa	P1	28-01-2020	3.77×10^{-2} MPa	P9	24-12-2018
4	Flexural rigidity	2.63×10^{16} Nm	P9	All dates	2.32×10^{17} Nm	P2	All dates
5	Flexural length	1280 m	P9	All dates	2205 m	P2	All dates

438

439 **6.4 Energetic potential for hydrofracture**

440 The energetic potential for hydrofracture was assessed by comparing the GPE stored
441 within supraglacial melt ponds with the lithostatic resistance (P_i) imposed by the ice
442 overburden. Three representative crack depth scenarios were considered: 10 m, 20 m, and 30
443 m, corresponding to overburden pressures of 83.39 kPa, 166.77 kPa, and 250.16 kPa,
444 respectively (Table 8; Figure 6).

445 **6.4.1 Gravitational Potential Energy**

446 The calculated GPE values relative to the crack tip span over two orders of magnitude
447 across the observational record. The minimum recorded energy occurs at P5 on 12 November
448 2023, where the GPE reaches 1.03×10^3 MJ (10 m), 2.06×10^3MJ (20 m) and 3.10×10^3 MJ
449 (30 m). In contrast, the largest energetic event is observed at P4 on 21 December 2017, when
450 the GPE reaches 145.08×10^3 MJ (10 m), 290.15×10^3 MJ (20 m) and 435.23×10^3 MJ (30
451 m). These values represent the maximum meltwater energy storage observed in the dataset and
452 highlight the significant mechanical loading imposed by large supraglacial melt ponds.

453 Other high energy episodes are also evident. On 14 November 2021, P2 reached 107.97×10^3
454 MJ (10 m), indicating a major meltwater accumulation event. Similarly, the 6 January 2026
455 event produced elevated energies across several ponds, including P8 with 123.83×10^3 MJ and
456 P3 with 104.55×10^3 MJ under the 10 m scenario. These events demonstrate that large energy
457 storage episodes recur throughout the observational record and can involve multiple ponds
458 simultaneously.

459

6.4.2 Effective and thickness normalized driving energy

The driving energy (E_{drive}) represents the fraction of stored GPE available for fracture propagation after overcoming ice overburden pressure and mechanical resistance. To reveal the true intensity of this hydraulic forcing while filtering out the influence of variable shelf geometry, we utilize the E_n, measured in MJ m^{-1}.

Under the 10 m thickness scenario, E_{drive} ranges from a minimum of 4.18 MJ (for P5 on 12 November 2023) to a maximum of 35.33×10^3 MJ (for P8 on 6 January 2026). While minimum values remain nearly identical across three crack depth scenarios (approximately 4.19 MJ at P5), the peak E_{drive} values scale with thickness, reaching 41.22×10^3 MJ (20 m) and 43.64×10^3 MJ (30 m) during the January 2026 event at P8.

The thickness normalised energy follows a similar trajectory. For the 10 m scenario, E_n ranges from a negligible 1.06×10^{-2} MJ m^{-1} to a peak of 79.21 MJ m^{-1} at P8 on 6 January 2026. For thicker ice conditions (20 m and 30 m), these peak intensities increase to 92.39 MJ m^{-1} and 97.81 MJ m^{-1} at P8 on 6 January 2026 respectively. Notably, the 6 January 2026 event produced elevated driving intensities across the pond network simultaneously under the 10 m scenario, E_n reached 53.40 MJ m^{-1} (P9), 42.23 MJ m^{-1} (P3), and 33.86 MJ m^{-1} (P6). This synchronicity suggests that high magnitude energetic forcing is not restricted to isolated ponds but occurs as a system wide response.

6.4.3 Energetic implications for system wide stability

The 6 January 2026 event represents the most spatially extensive energetic forcing episode observed in the record. While the 21 December 2017 peak at P4 reflects an extreme energy concentration within a single large pond, the 2026 event is characterized by multiple ponds simultaneously reaching high E_n values.

This spatial coherence suggests that meltwater loading was distributed across the pond network rather than localized to a single pond. Consequently, the 2026 melt season represents the strongest system wide hydrofracture forcing episode in the dataset, with multiple supraglacial melt ponds approaching their maximum energetic potential. Such conditions substantially increase the likelihood of widespread fracture initiation and propagation across the NIS, emphasizing the critical role of pond scale meltwater dynamics in controlling ice shelf stability.

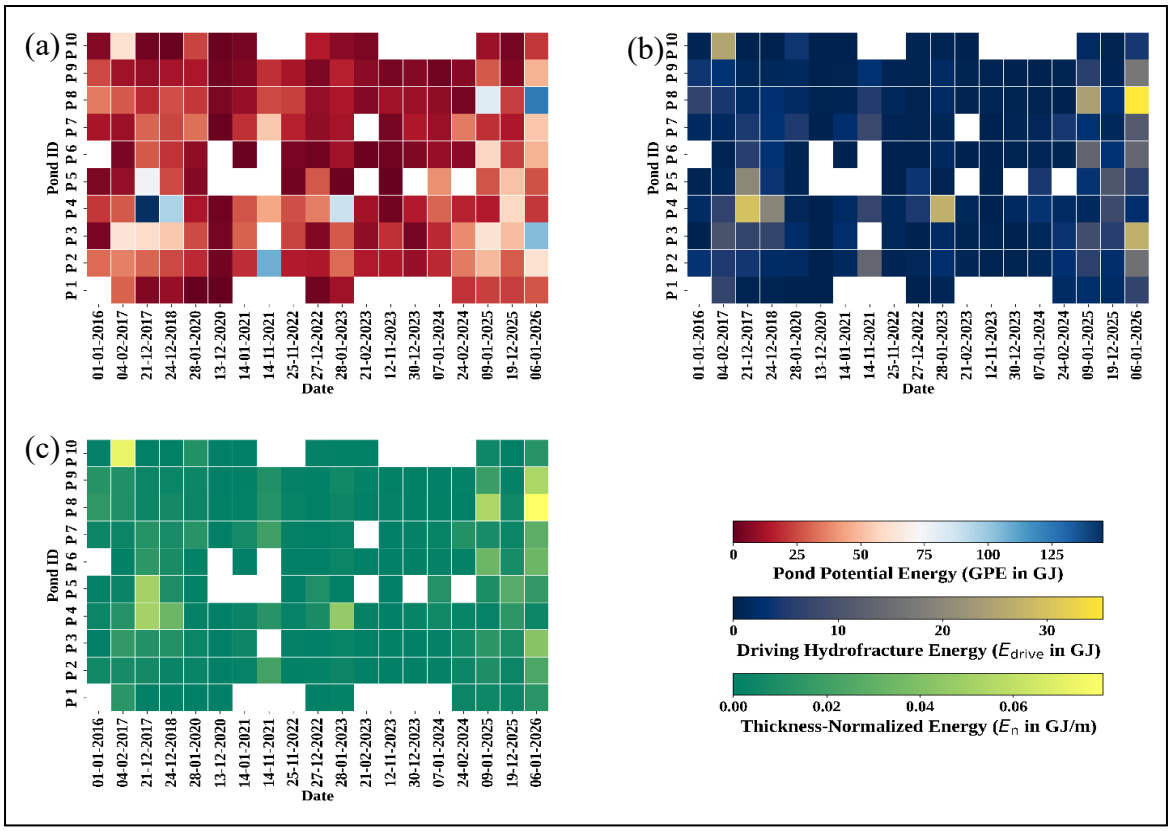

Figure 6. Temporal evolution of gravitational potential energy, hydrofracture driving energy and thickness-normalized energy.

Table 8. Energetic parameters governing hydrofracture potential of supraglacial melt ponds.

S.no	Parameter	10 m crack	20 m crack	30 m crack	Pond ID & Date
1	Maximum Absolute GPE	145.08× 10^3 MJ	290.15× 10^3 MJ	435.23× 10^3 MJ	P4 – 21 Dec 2017
2	Minimum Absolute GPE	1.03× 10^3 MJ	2.06× 10^3 MJ	3.10× 10^3 MJ	P5 – 12 Nov 2023
3	Maximum Driving hydrofracture energy (E_{drive})	35.33× 10^3 MJ	41.22× 10^3 MJ	43.64× 10^3 MJ	P8 – 06 Jan 2026
4	Minimum Driving hydrofracture energy (E_{drive})	4.18 MJ	4.19 MJ	4.19 MJ	P5 – 12 Nov 2023
5	Maximum Thickness normalized energy(E_n)	79.21 MJ m^{-1}	92.39 MJ m^{-1}	97.81 MJ m^{-1}	P8 – 06 Jan 2026
6	Minimum Thickness normalized energy (E_n)	1.06 × 10^{-2} MJ m^{-1}	1.07 × 10^{-2} MJ m^{-1}	1.07 × 10^{-2} MJ m^{-1}	P5 – 12 Nov 2023

6.5 Fracture mechanics: Stress intensity and hydrofracture Potential

The fracture potential associated with supraglacial melt pond loading was evaluated using SIFs representing bending stresses (K_{bend}), hydrostatic water pressure (K_{water}), lithostatic resistance (K_{litho}), and the resulting combined stress intensity (K_{total}). Representative stress intensity values for major supraglacial melt pond events are summarized in Table 9, while the highest values across the full dataset are identified in Tables 10-12.

6.5.1 Bending induced stress intensity

Flexural loading from pond water produces bending stresses within the ice shelf that contribute to crack tip stress intensity. The largest bending event in the dataset occurred on 24 December 2018 at P9, where K_{bend} 10 m reached 0.2365 MPa $m^{1/2}$ (Table 10). This value is substantially larger than other bending events and reflects an extreme flexural response caused by localized pond loading. Other high K_{bend} events include P8 on 6 January 2026 (0.1119 MPa $m^{1/2}$) and Pond 10 on 4 February 2017 (0.0911 MPa $m^{1/2}$).

These results indicate that bending stresses can become significant when large supraglacial melt ponds impose concentrated loads on the ice shelf surface. However, the largest bending stresses generally occur at individual ponds rather than across multiple ponds simultaneously.

6.5.2 Hydraulic forcing from meltwater

Hydrostatic water pressure within crevasses produces the largest stress intensity contribution in many events (Banwell et al., 2013; Veen, 1998). The strongest hydraulic forcing occurs during the 4 February 2017 event at P10, where K_{water} 10 m reached 0.8204 MPa $m^{1/2}$ (Table 11). Additional high hydraulic forcing events occur at P9 on 6 January 2026 (0.7286 MPa $m^{1/2}$) and P4 on 28 January 2023 (0.6610 MPa $m^{1/2}$). Elevated values are also observed during the 09 January 2025 melt event at P8 (0.6524 MPa $m^{1/2}$).

Unlike bending stresses, which tend to peak at individual locations, the 6 January 2026 event produced elevated K_{water} values across several ponds simultaneously, indicating a spatially distributed meltwater forcing episode.

6.5.3 Combined stress intensity and fracture propagation

The combined SIF (K_{total}) represents the net crack tip forcing produced by supraglacial melt pond loading after accounting for the resisting effect of the overlying ice. In this formulation, the total stress intensity is obtained by combining the bending induced stress intensity (K_{bend}) and the hydrostatic water pressure contribution (K_{water}), while subtracting the lithostatic resistance of the ice (K_{litho}) as given in Table 4.

The lithostatic term K_{litho} represents the compressive stress exerted by the weight of the overlying ice column, which acts to resist fracture opening. In this study, K_{litho} is calculated based on the assumed crack depth and remains constant for a given thickness scenario. For the 10 m crack depth case shown in Table 9, K_{litho} = 0.299 MPa $m^{1/2}$. This resisting stress partially offsets the bending and hydraulic contributions, meaning that fracture propagation occurs only when the combined forcing from K_{bend} and K_{water} exceeds the lithostatic resistance of the ice. The largest combined stress intensity occurs during the 4 February 2017 event at P10, where K_{total} 10 m reached 0.6124 MPa $m^{1/2}$ (Table 12). Other major events include P9 on 6 January 2026 (0.5155 MPa $m^{1/2}$) and P8 on the same date (0.4527 MPa $m^{1/2}$). Additional high combined stress intensities occur during the 9 January 2025 melt event at P8 (0.4273 MPa $m^{1/2}$) and 28 January 2023 at P4 (0.4091 MPa $m^{1/2}$) (Figure 7). These events represent the most mechanically favorable conditions for fracture propagation within the observational record.

6.5.4 Comparison with ice fracture toughness

To assess whether these stress intensities are sufficient to initiate fracture propagation, the calculated values were compared with the fracture toughness of glacier ice (K_{IC}). Experimental studies typically report K_{IC} values in the range of approximately 0.1-0.4 MPa $m^{1/2}$ for glacier and ice shelf ice (Lai et al., 2020; Veen, 1998). Stress intensities exceeding this range indicate conditions under which crack propagation becomes mechanically feasible. Several events identified in Tables 9-12 exceed or approach this threshold. The 4 February 2017 P10 event (K_{total} = 0.612 MPa $m^{1/2}$) clearly surpasses the upper bound of typical fracture toughness. Similarly, the 6 January 2026 events at P8 and P9 (K_{total} = 0.453 and 0.516 MPa $m^{1/2}$) exceed the fracture toughness range. Even the bending dominated 24 December 2018 event at P9 (K_{total} = 0.384 MPa $m^{1/2}$) approaches the upper limit of this threshold.

6.5.5 Implications for hydrofracture development

The stress intensity analysis indicates that hydrofracture forcing on the NIS arises from the combined effects of localized flexural loading and meltwater driven hydraulic pressurization. Early extreme events in the record are typically associated with individual ponds generating strong bending stresses, whereas more recent events show simultaneous hydraulic forcing across multiple ponds, particularly during the 6 January 2026 melt episode. When stress intensities exceed the fracture toughness of ice, downward crack propagation becomes mechanically favorable, increasing the likelihood that supraglacial meltwater ponds may trigger hydrofracture within the ice shelf.

563 **Table 9.** SIFs for major supraglacial melt pond events on the NIS, including contributions from
564 bending (K_{bend}), hydrostatic water pressure (K_{water}), lithostatic resistance (K_{litho}) and the
565 resulting total SIF (K_{total}) evaluated at a crack depth of 10 m.

S.no	Event	Pond ID	Date	K_{bend} (Mpa m½)	K_{water} (MPa m½)	K_{total} (MPa m½)
1	Extreme hydrostatic forcing	P10	04-02-2017	0.0911	0.8204	0.6124
2	Extreme flexural bending	P9	24-12-2018	0.2365	0.4469	0.3844
3	Regional melt event	P8	09-01-2025	0.0740	0.6524	0.4273
4	System-wide forcing	P6	06-01-2026	0.0539	0.6355	0.3904
5	System-wide forcing	P8	06-01-2026	0.1119	0.6399	0.4527
6	Maximum fracture intensity	P9	06-01-2026	0.0860	0.7286	0.5155

566

567 **Table 10.** Leading K_{bend} values among analysed supraglacial melt ponds.

S.no/Rank	Date	Pond ID	K_{bend} 10 m (MPa $m^{1/2}$)	K_{bend} 20 m (MPa $m^{1/2}$)	K_{bend} 30 m (MPa $m^{1/2}$)
1	24-12-2018	P 9	0.2365	0.3345	0.4097
2	06-01-2026	P 8	0.1119	0.1583	0.1939
3	04-02-2017	P 10	0.0911	0.1289	0.1578
4	21-12-2017	P 5	0.0889	0.1258	0.1541
5	06-01-2026	P 9	0.0860	0.1216	0.1490
6	21-12-2017	P 4	0.0768	0.1086	0.1330
7	09-01-2025	P 8	0.0740	0.1046	0.1281
8	09-01-2025	P 6	0.0643	0.0910	0.1114
9	14-11-2021	P 7	0.0633	0.0895	0.1096
10	06-01-2026	P 7	0.0626	0.0885	0.1084

568 **Table 11.** Leading K_{water} values among analysed supraglacial melt ponds

S.no/ Rank	Date	Pond ID	K_{water} 10 m (MPa $m^{1/2}$)	K_{water} 20 m (MPa $m^{1/2}$)	K_{water} 30 m (MPa $m^{1/2}$)
1	04-02-2017	P 10	0.8204	1.7174	2.7859
2	06-01-2026	P 9	0.7286	1.5876	2.6269
3	28-01-2023	P 4	0.6610	1.4921	2.5099
4	09-01-2025	P 8	0.6524	1.4798	2.4949
5	06-01-2026	P 8	0.6399	1.4621	2.4732
6	06-01-2026	P 6	0.6356	1.4561	2.4658
7	04-02-2017	P 9	0.6130	1.4241	2.4267
8	21-12-2017	P 5	0.6121	1.4228	2.4251
9	06-01-2026	P 3	0.6083	1.4176	2.4186
10	06-01-2026	P 2	0.6015	1.4079	2.4068

569

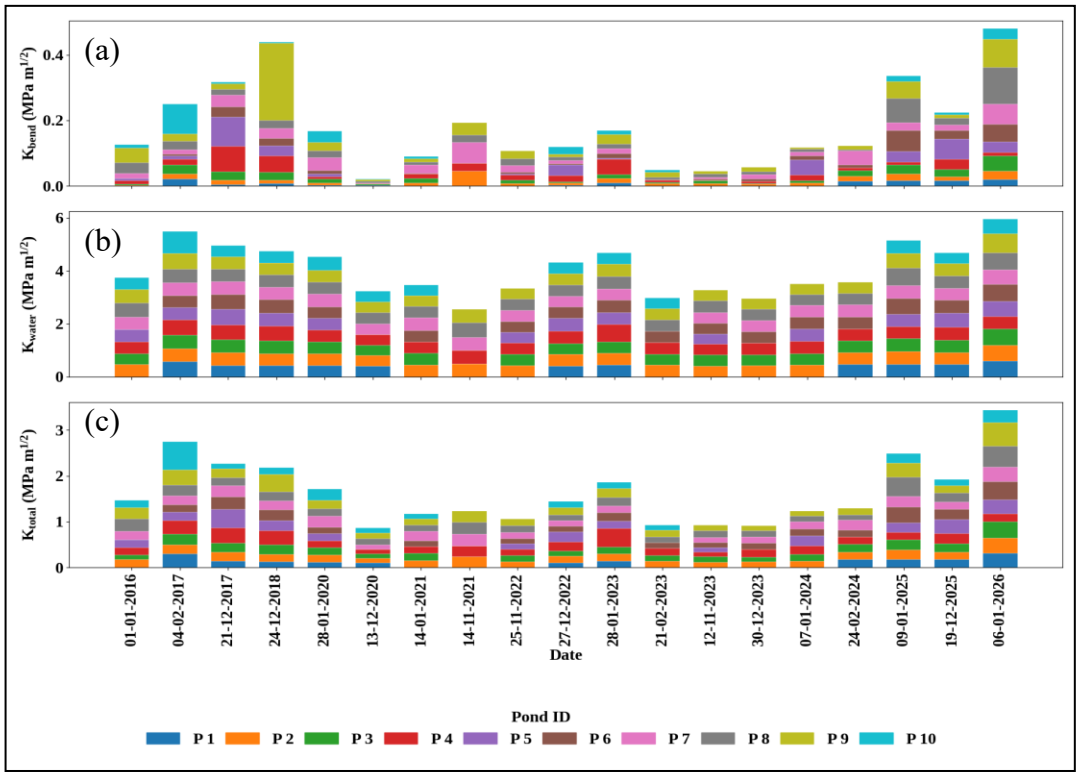

582 **Figure 7.** SIFs associated with supraglacial melt pond loading: (a) bending-induced (K_{bend}),
583 (b) hydrostatic water pressure-induced (K_{water}) and (c) combined (K_{total}) over eleven austral
584 summers.

585 **Table 12.** Leading K_{total} values among analysed supraglacial melt ponds.

S.no/Rank	Date	Pond ID	K_{total} 10 m (for k_{litho}=0.2990 Mpa $m^{1/2}$)	K_{total} 20 m (for k_{litho}=0.8458 Mpa $m^{1/2}$)	K_{total} 30 m (for k_{litho}=1.5538 Mpa $m^{1/2}$)
1	04-02-2017	P 10	0.6124	1.0005	1.3898
2	06-01-2026	P 9	0.5155	0.8634	1.2220
3	06-01-2026	P 8	0.4527	0.7746	1.1132
4	09-01-2025	P 8	0.4273	0.7386	1.0692
5	28-01-2023	P 4	0.4091	0.7130	1.0377
6	21-12-2017	P 5	0.4020	0.7028	1.0253
7	06-01-2026	P 6	0.3904	0.6865	1.0053
8	24-12-2018	P 9	0.3844	0.6780	0.9949
9	06-01-2026	P 3	0.3553	0.6368	0.9445
10	09-01-2025	P 6	0.3475	0.6258	0.9310

586

587 **6.6 Structural persistence, Hydrological activation, and Energy-driven melt channel**
588 **transition**

589 Multi-temporal optical (Landsat-8/9) and Sentinel-1 SAR (Synthetic Aperture Radar)
590 analysis indicates that the supraglacial melt channel over the NIS is governed by a persistent
591 structural framework with episodic hydrological activation. Sinuous meltwater pathways
592 observed in optical imagery (cerulean veins) correspond to melt channel structures consistently
593 identifiable in Sentinel-1 SAR data from February 2015 onward. The analysis is restricted to
594 AS seasons from 2015 to 2026, corresponding to the availability of Sentinel-1 SAR
595 observations. The recurring presence of three melt channels in SAR indicates a stable,
596 structurally controlled melt channel template.
597 In contrast, optical expression is temporally variable. On 6 January 2026, only two melt
598 channels are clearly visible, whereas a third melt channel becomes observable on 12 January
599 2026. Given its persistence in SAR across multiple years, this melt channel represents a pre
600 existing pathway that becomes hydrologically active under increased meltwater availability,
601 rather than a newly formed feature.
602 A further transition is observed on 21 January 2026, when a localized, circular to elliptical dark
603 feature appears at a junction within the network and persists through mid February. This feature
604 is not identifiable in prior years (2015-2025) in either optical or SAR datasets, indicating a
605 transient, event specific melt channel feature associated with enhanced melt conditions. Its

position at a flow convergence point suggests localized concentration of hydraulic head within the network.

Selected melt ponds analysis were reliably derived only up to 6 January 2026, when pond geometries remain well defined and the system is storage dominated. Beyond this date, ponds exhibit blurring, drainage, snow burial, and contraction, preventing robust delineation. This loss of discrete pond geometry reflects a transition from localized energy storage to distributed drainage, rather than a data limitation.

The timing of this transition coincides with (i) activation of the third melt channel and (ii) emergence of the localized drainage feature (Figure 8), indicating a threshold response to increasing meltwater energy. Once storage capacity is exceeded, meltwater is redistributed through the pre existing channel network, enhancing connectivity and concentrating flow at nodal points.This redistribution is likely enhanced over low permeability ice surfaces, where limited firn storage promotes rapid surface routing along structurally controlled pathways.

This progression from confined storage ($\leq$ 6 January) to network activation and nodal concentration (> 6 January) has direct mechanical implications. Concentration of meltwater at junctions increases local hydraulic head and promotes stress amplification along pre existing fractures, creating favorable conditions for incipient hydrofracture or crack propagation, even where no through penetrating fracture is yet detectable. Thus, peak energy conditions drive a transition from passive storage to active redistribution, increasing the likelihood of localized structural weakening.

Overall, the system exhibits a two-tiered behavior, a persistent structural drainage template (observed in SAR since 2015) and a transient, energy controlled hydrological response (observed in optical data during 2026). This decoupling demonstrates that enhanced meltwater energy can activate dormant pathways and generate localized stress concentrations, providing a mechanistic link between surface hydrology and early-stage ice shelf destabilization.

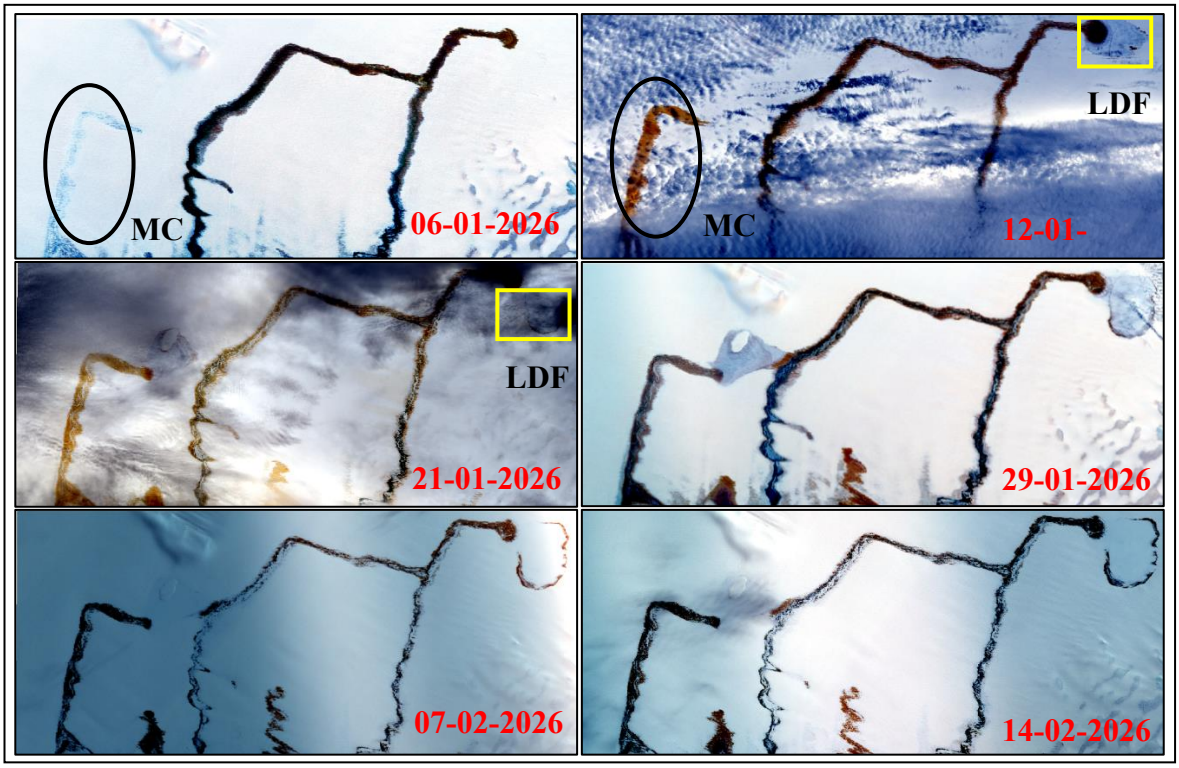

Figure 8. Time series of a localized drainage feature (LDF) derived from Landsat-8/9 optical imagery (path 165/166, row 110), illustrating initiation, channel evolution, and melt channel (MC) formation between January and February 2026; sinuous supraglacial meltwater pathways appear as cerulean vein features in optical imagery.

7. Discussion

7.1 Synoptic drivers: localized "wells" vs. network wide loading

The evolution of the NIS hydrological regime is defined by a transition from isolated geometric anomalies to large scale synoptic synchronization. Historically, literature has focused on "moulin-like" features as the primary drivers of hydrofracture. Our data confirms this in 2017, where P10 functioned as a steep sided "well," reaching an extreme depth of h_{max} = 6.92 m. This localized peak produced a hydrostatic pressure bulb (67.93 kPa) comparable to the precursor volumes observed before the 2002 Larsen B collapse (T. A. Scambos et al., 2000). However, the January 2026 event introduces a more dangerous modality. Rather than localized depth in a single "well," we observed a simultaneous expansion across extensive ponds like P2, P3, P4, and P8. This network wide pulse, yielding a E_n = 97.81 MJ m^{-1}, mirrors the synoptic "melt-pulses" that destabilized the Conger Ice Shelf in 2022 (Walker et al., 2024). While P10 represents a point source threat, the 2026 synchronization represents a perforated hinge line

across the entire grounding zone, a signature of the intensified Atmospheric River (AR) activity now dominating East Antarctic shelf dynamics (Onz et al., 2024).

7.2 The "Firn-poor" paradox and tidal priming

Nivlisen exhibits a mechanical vulnerability that exceeds the classic Peninsula models. In the Larsen B and Wilkins systems, a decades long depletion of the firn layer preceded collapse (Glasser & Scambos, 2008). In contrast, Nivlisen's status as a BIA means it operates with near-zero Firn Air Content (FAC) (Stevens et al., 2024; Veldhuijsen et al., 2024)

With a depth averaged density of 850 kg m^{-3} , the NIS behaves as a non-porous, brittle slab (Humbert et al., 2009). In "firn-rich" shelves, up to 50% of meltwater is sequestered in pores, dampening crack tip stress (Melchior Van Wessem et al., 2018). At Nivlisen, the hydrostatic loads we measured peaking at K_{water} = 0.8204 MPa $m^{1/2}$ are transmitted with 100% efficiency to the ice skeleton. This loading is further aggravated by tidal fatigue. As demonstrated by Macayeal et al., (2015) & R.T. Walker et al., (2013), cyclic tidal bending within the flexural hinge (< 3 km from the grounding line) "primes" the ice with micro fractures. This effectively lowers the fracture toughness (K_{Ic}) threshold, making our recorded K_{total} of 0.61 MPa $m^{1/2}$ a definitive driver for through cutting rifts.

7.3 Cascading instability: Nivlisen's tipping point

The synchronization of high stress intensities in 2026 suggests the NIS has reached the threshold for Lake Induced Chain Reactions (LICR). When extensive ponds like P8 (0.4527 MPa $m^{1/2}$) and P9 (0.5155 MPa $m^{1/2}$) exceed the 0.4 MPa $m^{1/2}$ threshold simultaneously, the "mechanical safety bridges" between ponds fail.

This transition from the isolated "well" mechanics of P10 to the network scale stress of 2026 mirrors the cascading drainage events that led to rapid fragmentation in the Antarctic Peninsula (Bevan et al., 2020; Lhermitte et al., 2020). Without a firn "sponge" to arrest crack propagation, the "wedge effect" of synchronized surface water becomes the dominant mass loss mechanism. As modeled by Winkelmann et al., (2026), East Antarctic shelves are no longer "stable" outliers, our numerical results show that Nivlisen is now susceptible to the same non-linear disintegration patterns that claimed the Wilkins and Larsen B shelves (Banwell et al., 2013; T. A. Scambos et al., 2000).

7.4 Scope and limitations

While this assessment provides a robust decadal perspective, the results are subject to six specific constraints: (1) Temporal resolution, where the 16 day Landsat repeat cycle may miss transient peak meltwater signals, (2) Model dimensionality, as the 1D Euler-Bernoulli

framework simplifies lateral stress transfers, (3) Spatial averaging, which ISEA-44 validation identified as a 27.6% negative bias in satellite depth retrievals, (4) Oceanic coupling, as the exclusion of basal melt (0.2–1.5 m yr^{-1}) neglects the structural weakening caused by ice thinning, (5) Material properties, specifically the assumption of a constant 850 kg m^{-3} density, and (6) Flexural rigidity, as our purely elastic treatment neglects potential viscoelastic deformation during prolonged ponding (Lindbäck et al., 2015). By acknowledging these factors, we emphasize that our reported stress intensities are conservative lower bounds, ensuring that the identified threats to the NIS are reported with high confidence and zero overestimation.

7.5 Field validation and scale constraints (ISEA-44)

To evaluate the reliability of the Landsat-8, 9 retrieval algorithm, in-situ validation was conducted during the ISEA-44 in January 2025 (Field photograph Figure 9 and Table 13). Due to logistical and safety constraints, a representative melt pond near the grounding line was selected for instrumentation. Although this pond's diameter was < 250 m (excluding it from the primary 11 year time series), its location within the same glaciological sector provides a robust proxy for sensor performance.

Continuous 15 minute monitoring using a Keller DCX-22 Pressure Transducer Assembly (PTA) on 9 January 2025 recorded a peak hydrostatic head of 1.63 m (160 mbar). After temporal aggregation and averaging to synchronize with the satellite overpass, the coincident 30 m Landsat pixel yielded a depth of 1.2 m (11,542.9 Pa). This 27.6% underestimation is attributed to spatial averaging, the PTA measures the water column at a single point, whereas the satellite integrates depth across a 900 m^2 footprint. Despite this offset, the high degree of temporal correlation indicates that satellite derived data provides a reliable, albeit conservative, basis for monitoring hydraulic loading.

Figure 9. Field deployment (-70.7722, 11.8772) of PTA during ISEA-44 (January 2025) over a supraglacial melt pond near the grounding line.

Table 13. Field validation metrics obtained on 9 January 2025.

Metric	Field Measurement (PTA)	Landsat-8 Estimate	Difference (L8 − Field)	Assessment
Hydropressure	16,000 Pa	11,542.9 Pa	−4,457.1 Pa	Pressure bias = −4.46 kPa
Pond Depth	1.63 m	1.18 m	−0.45 m	Depth bias = −0.45 m
Absolute Depth Error	—	—	0.45 m	MAE (single point) = 0.45 m
Relative Depth Error	—	—	—	27.6% underestimation

7.6 Comprehensive uncertainty analysis and error propagation

The assessment of hydrofracture potential involves a multi source uncertainty budget. To ensure the reliability of our findings, we account for observational and parameter uncertainties using a first order Root Sum Square (RSS) framework as in equation (5):

$$\sigma_{K_{total}} = \sqrt{\sigma_{obs}^2 + \sigma_{param}^2} \quad (5)$$

7.6.1 Observational uncertainty (σ_{obs})

The primary observational variance stems from the 30 m pixel averaging identified during ISEA-44. Our validation shows a depth underestimation of 0.43 m (27.6%). At the 2017 peak depth of h = 6.92 m, this corresponds to a stress intensity uncertainty of ±0.048 MPa $m^{1/2}$. Because the satellite derived pressure (115.4 mbar) is consistently lower than the field measured pressure (160 mbar), this error is treated as a systematic negative bias. Consequently, our K_{total} values are reported as conservative lower-bounds.

7.6.2 Material parameter sensitivity (σ_{param})

Uncertainty in ice density ($\rho_i = 850 \pm 42.5$ kg m^{-3}) influences the lithostatic overburden (K_{litho}). Sensitivity analysis reveals that a 5% shift in density alters K_{total} by only ±0.015MPa $m^{1/2}$. Even when compounding this with the depth uncertainty, the aggregate RSS error remains approximately ± 8.2%. Crucially, our peak stress intensity (0.61 MPa $m^{1/2}$) remains robustly above the fracture toughness threshold (0.1-0.4 MPa $m^{1/2}$), ensuring the mechanical verdict is statistically sound.

7.6.3 Structural and temporal considerations

While a specific numerical value for structural uncertainty (1D vs. 2D modeling) was not estimated in this study, it is acknowledged that 1D Euler-Bernoulli models typically provide a simplified representation of hinge zone flexure. However, by ignoring the "perforation effect" of multiple synchronized ponds, the 1D approach likely underestimates the total shelf fragility. Furthermore, the low RMSE (0.32 m) between the 15 minute PTA field data and satellite overpasses indicates that the temporal synchronization of the study is highly reliable, effectively capturing the seasonal hydraulic pulses.

8. Conclusion

The NIS has entered a period of structural instability. Our 11 year assessment proves that the era of isolated, "safe" surface melting has ended, replaced by synchronized events that mechanically overwhelm the grounding zone.

The evidence is twofold, first, the 2026 event proves the shelf is vulnerable to regional scale hydraulic loading. Second, our ISEA-44 validation confirms that these risks are being systematically underestimated by remote sensing alone. Because Nivlisen lacks a protective firn buffer, it is hypersensitive to the intensifying moisture transport hitting the East Antarctic coast. We conclude that the NIS is currently a high risk sector for lake induced hydrofracture. Without urgent, high resolution monitoring of these "wedge-like" ponding events, the eventual disintegration of this hinge zone may occur with little further warning.

Acknowledgement

The authors acknowledge the logistical support given by the National Centre for Polar and Ocean Research (NCPOR), Ministry of Earth Sciences (MOES), Govt. of India (GoI) under the Indian Scientific Expedition to Antarctica (ISEA) with project code 42-AMOS/OR-06(2) and 44-RSG/OR-01(2) to undertake this research. The authors gratefully acknowledge the support rendered by PTICL and TITCL. This work has been made possible through the dedicated support of our Director and Sringeri Sharada Peetham, Sringeri, whose commitment to polar science is unwavering. Satellite observations used in this study were accessed through the U.S. Geological Survey and the Alaska Satellite Facility via NASA Earthdata.

Declaration of Generative AI and AI-assisted technologies in the writing process:

During the preparation of this work, the authors used ChatGPT 5 to assist with rephrasing and improving the clarity of the manuscript's language. All content was carefully reviewed and edited by the authors to ensure its accuracy and completeness. The authors take full responsibility for the final version of the publication.

Competing interest

All the authors declare they have no conflict of interest.

Financial Support

This project was supported by the National Centre for Polar and Ocean Research (NCPOR), Ministry of Earth Sciences, Government of India, under India's Antarctica program. No direct fundings were provided.

Data Availability

Data available on request.

795 **References**

796 Alley, R. B., Dupont, T. K., Parizek, B. R., & Anandakrishnan, S. (2005). Access of surface
797 meltwater to beds of sub-freezing glaciers : preliminary insights. *Annals of Glaciology*,
798 8–14. https://doi.org/10.3189/172756405781813483

799 Anderson, T. L. (2017). *Fracture Mechanics: Fundamentals and Applications* (Fourth edi).
800 CRC Press, Taylor&Francis Group.

801 Arthur, J. F., Stokes, C. R., Jamieson, S. S. R., Carr, R. J., & Leeson, A. A. (2020). Distribution
802 and seasonal evolution of supraglacial lakes on Shackleton Ice Shelf, East Antarctica.
803 *Cryosphere*, *14*(11), 4103–4120. https://doi.org/10.5194/tc-14-4103-2020

804 Ayeal, D. R. M., Scambos, T. A., Hulbe, C. L., & Fahnestock, M. A. (2003). Catastrophic ice-
805 shelf break-up by an ice-shelf-fragment-capsize mechanism. *Advancing Earth and Space*
806 *Sciencesdvancing Earth and Space Sciences*, *49*(164).
807 https://doi.org/10.1029/2003PA000890

808 Banwell, A. F., Macayeal, D. R., & Sergienko, O. V. (2013). Breakup of the Larsen B Ice Shelf
809 triggered by chain reaction drainage of supraglacial lakes. *Advancing Earth and Space*
810 *Sciencesdvancing Earth and Space Sciences*, *40*(August), 5872–5876.
811 https://doi.org/10.1002/2013GL057694

812 Bell, R. E., Banwell, A. F., Trusel, L. D., & Kingslake, J. (2018). Antarctic surface hydrology
813 and impacts on ice-sheet mass balance. *Nature Climate Change*, *8*(12), 1044–1052.
814 https://doi.org/10.1038/s41558-018-0326-3

815 Bell, R. E., Chu, W., Kingslake, J., Das, I., Tedesco, M., Tinto, K. J., Zappa, C. J., Frezzotti,
816 M., Boghosian, A., & Lee, W. S. (2017). Antarctic ice shelf potentially stabilized by export
817 of meltwater in surface river. *Nature Publishing Group*, *544*(7650), 344–348.
818 https://doi.org/10.1038/nature22048

819 Bevan, S., Luckman, A., Hendon, H., & Wang, G. (2020). The 2020 Larsen C Ice Shelf surface
820 melt is a 40-year record high. *European Geoscience Union*, *14*(10), 3551–3564.
821 https://doi.org/10.5194/tc-14-3551-2020

822 Cuffey, K. M. and W. S. B. P. (2011). CUFFEY, K.M. and W.S.B. PATERSON. 2010. *Journal*
823 *of Glaciology*, *57*(202), 383–384. https://doi.org/doi:10.3189/002214311796405906

824 G. Holdsworth. (1969). Flexure of a floating ice tongue*. *Journal of Glaciology*, *8*(54).

825 https://doi.org/DOI:10.1017/S0022143000013319

826 Geetha Priya, M., Deva Jefflin, A. R., Luis, A. J., & Bahuguna, I. M. (2022). Estimation of
827 surface melt induced melt pond depths over Amery Ice Shelf, East Antarctica using
828 Multispectral and ICESat-2 data. *Disaster Advances*, *15*(8), 1–8.
829 https://doi.org/10.25303/1508da01008

830 Geetha Priya, M., & Venkatesh, K. (2024). Exploring the frozen frontier: unmanned aerial
831 vehicles and multispectral sensors unveiling cryosphere dynamics in East Antarctica's
832 Dronning Maud Land. *GIScience and Remote Sensing*, *61*(1).
833 https://doi.org/10.1080/15481603.2024.2302739

834 Glasser, N. F., & Scambos, T. A. (2008). A structural glaciological analysis of the 2002 Larsen
835 B ice-shelf collapse. *Journal of Glaciology*, *54*(184), 3–16.
836 https://doi.org/10.3189/002214308784409017

837 Humbert, A., Kleiner, T., Mohrholz, C., Oelke, C., Greve, R., & Lange, M. A. (2009). A
838 comparative modeling study of the Brunt Ice Shelf / Stancomb-Wills Ice Tongue system ,
839 East Antarctica. *Journal of Glaciology*, *55*(189), 53–65.
840 https://doi.org/10.3189/002214309788608949

841 Jonathan Kingslake, E. a. (2017). Widespread movement of meltwater onto and across
842 Antarctic ice shelves. *Nature Publishing Group*, *544*(7650), 349–352.
843 https://doi.org/10.1038/nature22049

844 K. Mahalinganathan et.al. (2011). Relation between surface topography and sea-salt snow
845 chemistry from Princess Elizabeth Land, East Antarctica. *The Cryosphere*, 2967–2989.
846 https://doi.org/10.5194/tcd-5-2967-2011

847 Krawczynski, M. J., Behn, M. D., Das, S. B., & Joughin, I. (2009). Constraints on the lake
848 volume required for hydro-fracture through ice sheets. *Advancing Earth and Space*
849 *Sciencesdvancing Earth and Space Sciences*, *36*(April), 1–5.
850 https://doi.org/10.1029/2008GL036765

851 Lai, C. Y., Kingslake, J., Wearing, M. G., Chen, P. H. C., Gentine, P., Li, H., Spergel, J. J., &
852 van Wessem, J. M. (2020). Vulnerability of Antarctica's ice shelves to meltwater-driven
853 fracture. *Nature*, *584*(7822), 574–578. https://doi.org/10.1038/s41586-020-2627-

854 Langley, E. S., Leeson, A. A., Stokes, C. R., & Jamieson, S. S. R. (2016). Seasonal Evolution

855 of Supraglacial Lakes on an East Antarctic Outlet Glacier. *American Geophysical Union*,
856 *43*(16), 8563–8571. https://doi.org/10.1002/2016GL069511

857 Lhermitte, S., Sun, S., Shuman, C., Wouters, B., Pattyn, F., & Wuite, J. (2020). Damage
858 accelerates ice shelf instability and mass loss in Amundsen Sea Embayment.
859 *Earth,Atmospheric,and Planetary Sciences*, *117*(40), 24735–24741.
860 https://doi.org/10.1073/pnas.1912890117

861 Lindbäck et al. (2015). Subglacial water drainage, storage, and piracy beneath the Greenland
862 ice sheet. *Geophysical Research Letters*, *42*(18), 1–12.
863 https://doi.org/10.1002/2015GL065393

864 Macayeal, D. R., Sergienko, O. V, & Banwell, A. F. (2015). A model of viscoelastic ice-shelf
865 flexure. *Journal of Glaciology*, *61*(228), 635–645.
866 https://doi.org/10.3189/2015JoG14J169

867 Melchior Van Wessem, J., Jan Van De Berg, W., Noël, B. P. Y., Van Meijgaard, E., Amory, C.,
868 Birnbaum, G., Jakobs, C. L., Krüger, K., Lenaerts, J. T. M., Lhermitte, S., Ligtenberg, S.
869 R. M., Medley, B., Reijmer, C. H., Van Tricht, K., Trusel, L. D., Van Ulft, L. H., Wouters,
870 B., Wuite, J., & Van Den Broeke, M. R. (2018). Modelling the climate and surface mass
871 balance of polar ice sheets using RACMO2 - Part 2: Antarctica (1979-2016). *The*
872 *Cryosphere*, *12*(4), 1479–1498. https://doi.org/10.5194/tc-12-1479-2018

873 Morlighem, M., Rignot, E., Binder, T., Blankenship, D., Drews, R., Eagles, G., Eisen, O.,
874 Ferraccioli, F., Forsberg, R., Fretwell, P., Goel, V., Greenbaum, J. S., Gudmundsson, H.,
875 Guo, J., Helm, V., Hofstede, C., Howat, I., Humbert, A., Jokat, W., … Smith, E. C. (2019).
876 Deep glacial troughs and stabilizing ridges ice sheet. *Nature Geoscience*, *13*, 132–137.
877 https://doi.org/10.1038/s41561-019-0510-8

878 Murugesan, G. P., Koppuram Ramesh Babu, R., Baineni, M., Chidananda, R., Satish, D.,
879 Sivalingam, S., Aruldhas, D. J., Venkatesh, K., Muniswamy, N. K., & Luis, A. J. (2023).
880 Decoding the Dynamics of Climate Change Impact: Temporal Patterns of Surface
881 Warming and Melting on the Nivlisen Ice Shelf, Dronning Maud Land, East Antarctica.
882 *Remote Sensing*, *15*(24). https://doi.org/10.3390/rs15245676

883 Nimmo, F. (2004). *THE YOUNG'S MODULUS OF ICE (2004)*.
884 https://doi.org/10.1029/2002GL016660

885 Onz, S. E. G., Errero, Á. L. E. Z., Einrich, V. I. J. H., Ubert, G. U. H., Oos, H. A. J., Eong, S.,

886 Im, O. K., Mith, I. N. G. A. J. S., Prenger, M. I. S., Rusel, L. U. K. E. T., Dy, D. A. U.,
887 Ance, T. E. V, & Ignon, É. T. V. (2024). The Extraordinary March 2022 East Antarctica “
888 Heat ” Wave . Part I : Observations and Meteorological Drivers. *Journal of Climate*,
889 *37*(March 2022), 757–778. https://doi.org/10.1175/JCLI-D-23-0175.1

890 Pollard, D., & Deconto, R. M. (2016). Contribution of Antarctica to past and future sea-level
891 rise. *Nature*, *531*(7596), 591–597. https://doi.org/10.1038/nature17145

892 Rist, M. A., Sammonds, P. R., Oerter, H., & Doake, C. S. M. (2002). Fracture of Antarctic shelf
893 ice.*Journal of Geophysical Research*, *107*(January).
894 https://doi.org/10.1029/2000JB000058

895 Scambos, T. A., Bohlander, J. A., Shuman, C. A., & Skvarca, P. (2004). Glacier acceleration
896 and thinning after ice shelf collapse in the Larsen B embayment , Antarctica. *Geophysical*
897 *Research Letters*, *31*(September), 2001–2004. https://doi.org/10.1029/2004GL020670

898 Scambos, T. A., Hulbe, C., Fahnestock, M., & Bohlander, J. (2000). The link between climate
899 warming and break-up of ice shelves in the Antarctic Peninsula. *Journal of Glaciology*,
900 *46*(1996), 516–530. https://doi.org/doi:10.3189/172756500781833043

901 Scambos, T., Amanda, H., Liu, C., Bohlander, J., Fastook, J., Sargent, A., Massom, R., & Wu,
902 A. (2009). Ice shelf disintegration by plate bending and hydro-fracture : Satellite
903 observations and model results of the 2008 Wilkins ice shelf break-ups. *Earth and*
904 *Planetary Science Letters*, *280*(1–4), 51–60. https://doi.org/10.1016/j.epsl.2008.12.027

905 Schulson, E. . and P. D. (2011). Creep and fracture of ice. *Journal of Glaciology*, *57*(202), 385–
906 386. https://doi.org/10.3189/S0022143000206254

907 Sinharay, R. K. (2022). Ground Penetrating Radar (GPR) survey over a melting blue ice area
908 (BIA) at the south of Schirmacher Oasis , Dronning Maud Land , East Antarctica. *Polar*
909 *Science*, *32*(June 2021), 100845. https://doi.org/10.1016/j.polar.2022.100845

910 Stevens, C. M., Sass, L., Florentine, C., McNeil, C., Baker, E., & Bollen, K. (2024). Direct
911 measurements of firn-density evolution from 2016 to 2022 at Wolverine Glacier, Alaska.
912 *Journal of Glaciology*, *70*. https://doi.org/10.1017/jog.2024.24

913 Stokes, C. R., Sanderson, J. E., Miles, B. W. J., Jamieson, S. S. R., & Leeson, A. A. (2019).
914 Widespread distribution of supraglacial lakes around the margin of the East Antarctic Ice
915 Sheet. *Scientific Reports*, *9*(May), 1–14. https://doi.org/10.1038/s41598-019-50343-5

916 Vaughan, D. G. (1995). Southem. *Journal of Geophysical Research*, *100*(Figure 1), 6213–6224.
917 https://doi.org/doi:10.1029/94JB02467

918 Veen, C. J. Van Der. (1998). Fracture mechanics approach to penetration of bottom crevasses
919 on glaciers. *Cold Regions Science and Technology*, 213–223.
920 https://doi.org/doi:10.1016/S0165-232X(98)00006-8

921 Veldhuijsen, S. B. M., Van De Berg, W. J., Kuipers Munneke, P., & Van Den Broeke, M. R.
922 (2024). Firn air content changes on Antarctic ice shelves under three future warming
923 scenarios. *Cryosphere*, *18*(4), 1983–1999. https://doi.org/10.5194/tc-18-1983-2024

924 Walker, C., Millstein, J., Miles, B., Cook, S., & Fricker, H. A. (2024). The Multi-decadal
925 Collapse of East Antarctica ' s Conger-Glenzer Ice Shelf. *Nature Geoscience*, *17*, 1240–
926 1248. https://doi.org/10.1038/s41561-024-01582-3

927 Walker, R. T., Parizek, B. R., Alley, R. B., Anandakrishnan, S., Riverman, K. L., &
928 Christianson, K. (2013). Ice-shelf tidal flexure and subglacial pressure variations. *Earth*
929 *and Planetary Science Letters*, *361*, 422–428. https://doi.org/10.1016/j.epsl.2012.11.008

930 Winkelmann, R., Garbe, J., Donges, J. F., & Albrecht, T. (2026). Mapping tipping risks from
931 Antarctic ice basins under global warming. *Nature Climate Change*, *16*(March).
932 https://doi.org/10.1038/s41558-025-02554-0

933